Economically viable electrocatalytic ethylene production with high yield and selectivity

Bo-Hang Zhao
Tianjin University https://orcid.org/0000-0002-0683-4650
Fanpeng Chen
Tianjin University https://orcid.org/0000-0003-2684-3180
Mengke Wang
Tianjin University https://orcid.org/0000-0001-6373-451X
Chuanqi Cheng
Tianjin University https://orcid.org/0000-0002-3366-8395
Yongmeng Wu
Tianjin University https://orcid.org/0000-0003-2778-6018
Cuibo Liu
https://orcid.org/0000-0002-9578-8173
Yifu Yu
Tianjin University https://orcid.org/0000-0002-7927-1350
Bin Zhang (bzhang@tju.edu.cn)
Tianjin University https://orcid.org/0000-0003-0542-1819

Article

Keywords:

Posted Date: February 14th, 2023

DOI: https://doi.org/10.21203/rs.3.rs-1602837/v1

Version of Record: A version of this preprint was published at Nature Sustainability on March 9th, 2023.
See the published version at https://doi.org/10.1038/s41893-023-01084-x.

Abstract

Electrocatalytic semihydrogenation of acetylene provides a clean pathway to produce ethylene (C_2H_4), one of the most widely used petrochemical feedstocks, but its performance is still well below that of the thermocatalytic route, leaving its practical feasibility questionable. Here our techno-economic analysis shows that this process becomes profitable if the Faraday efficiency (FE) exceeds 85% at a current density of 0.2 A cm^{-2}. As a result, we design a Cu nanoparticle catalyst with coordinatively unsaturated sites to steer the reaction towards these targets. Remarkably, our electrocatalyst synthesized on gas diffusion layer-coated carbon paper enables a high C_2H_4 yield rate of 70.15 mmol mg^{-1} h^{-1} and a FE of 97.7% at an industrially relevant current density of 0.5 A cm^{-2}. Combined characterizations and calculations reveal that such performance can be attributed to a favorable combination of a higher energy barrier for coupling of active hydrogen atoms (H*) and weak absorption of *C_2H_4. The former serves to suppress the competitive hydrogen evolution reaction, whereas the latter avoids overhydrogenation and C-C coupling. Further life cycle assessment evidences the economic feasibility and sustainability of the process. Our work suggests a way towards rational design and manipulation of nanocatalysts that could find wider and greener catalytic applications.

Introduction

Ethylene (C_2H_4), one of the vital feedstocks to produce most commodity chemicals, such as ethanol, glycols, and vinyl chloride[1], is of great significance in the chemical industry[2,3]. At present, traditional C_2H_4 production is excessively dependent on the cracking of oil and shale gas[4-6]. The limited petroleum reserves, high energy consumption, and easy deactivation problems of the cracking process make it highly desirable to seek a petroleum-independent production process for C_2H_4 [7-9]. Recently, acetylene (C_2H_2) has been efficiently produced through the arc-plasma process of coal[10-13]. Thus, semihydrogenation of coal-derived acetylene to ethylene (SAE) offers a promising petroleum-independent route to C_2H_4 production[14]. Although the thermocatalytic SAE process has made great advances, high temperature and pressure are still needed, leading to high energy consumption[15,16]. In addition, the excess use of hydrogen (H_2) and inevitable separation make the process more costly. In these regards, electrocatalytic SAE (ESAE) using water (H_2O) as the hydrogen source under ambient conditions is a promising petroleum-independent and environmentally friendly alternative/complementary for C_2H_4 production. However, its advance is still hindered by the severe hydrogen evolution reaction (HER), resulting in a relatively low ethylene yield and Faraday efficiency (FE)[17]. At present, the deficiency of techno-economic analysis (TEA) makes the target of the ESAE process unclear. Thus, performing TEA of the as-proposed technique and developing efficient catalytic materials to suppress the competitive HER and produce ethylene with high efficiency under industrially relevant current densities is urgently needed.

Copper (Cu)-based materials have been proven to be excellent catalyst candidates for the SAE process to remove C_2H_2 impurities from C_2H_4-rich gas streams and selective semihydrogenation of alkynes[18,19].

Very recently, Deng and coworkers reported the possibility of C_2H_4 production over Cu macroparticles with a size of 1-2 mm through the ESAE process[17]. However, the FE of C_2H_4 is highly dependent on the precise control of the current density. The FE of C_2H_4 above 60 mA cm^{-2} is lower than 50%, which is difficult for the large-scale production of C_2H_4. Thus, it is highly significant to design an efficient catalyst for C_2H_4 production with high FE at industrially relevant current densities (≥0.1 A cm^{-2}). In comparison with bulk and macrosized Cu, Cu nanostructures with a diameter of approximately 5 nm are both experimentally[20,21] and theoretically[22] proven to be more favorable in H_2 dissociation in thermocatalytic hydrogenation reactions due to unsaturated coordination[23,24]. Conversely, unsaturated Cu nanoparticles are supposed to impede the coupling of active atomic hydrogen atoms (H^*) to release H_2 in the ESAE process, lowering the selectivity and FE of undesirable H_2. In this regard, low-coordination Cu nanostructures are promising electrocatalysts for C_2H_4 production through the ESAE process at an industrially relevant current density. In addition, a gas-diffusion electrode is necessary for continuous synthesis[25-27]. Furthermore, direct growth of nanosized catalysts on gas diffusion electrodes (GDEs) can not only avoid the use of any polymer binders[28] or difficult-to-remove surfactants,[29] which may block the gas diffusion channels but also enhance the bonding strength between the catalysts and GDEs, leading to improved mass transfer and electrode durability[30]. However, the direct synthesis and use of low-coordination Cu nanoparticles on a gas diffusion layer-coated carbon paper (GDL-CP) electrode for industrialization-oriented ethylene production is still a highly challenging task.

Herein, a preliminary TEA of this ESAE process is performed to determine the profitable target of a ≥85% C_2H_4 FE at a current density of ≥0.2 A cm^{-2}. GDL-CP-supported Cu nanoparticles with rich unsaturated sites (denoted as ED-Cu NPs) are theoretically and experimentally reported to be an outstanding electrocatalyst for the ESAE process. ED-Cu NPs deliver a C_2H_4 FE of 97.7% at a current density of 0.5 A cm^{-2} with a single-pass C_2H_2 conversion rate of 12.4%, and a C_2H_4 production rate of 70.15 mmol mg^{-1} h^{-1}, greatly outperforming the commercial Cu counterpart and the electrodeposited Cu macrosized particles. Cu nanoparticles with rich unsaturated sites are revealed to promote active hydrogen atom (H*) formation and suppress competitive HER and acetylene overhydrogenation, thus accelerating ethylene production. Moreover, the in situ spectroscopic characterization reveals that the ESAE process follows the H^* addition mechanism. Subsequently, the kinetic isotope effect and density functional theory (DFT) calculation results suggest that sufficient H^* on ED-Cu NPs enables high ethylene FE in a wide window of current densities. Furthermore, a cradle-to-gate life cycle assessment (LCA) confirms the sustainability of the ESAE strategy.

Results

Theoretical calculations assisted design of electrocatalysts

First, a TEA of the proposed ESAE process for C_2H_4 production at the industrial manufacturing level is simulated based on the model reported recently (Supplementary Note 1) [31,32] . The parameters used in the TEA are reasonably assumed according to the reported state-of-the-art performance data [11] and our preliminary experimental results (Supplementary Figs. 1, 2 and Supplementary Table 1). The ESAE process is profitable when the current density and FE of C_2H_4 are higher than 0.2 A cm^{-2} and 85% at the given electricity price of 0.03 \$ kWh^{-1} (Fig. 1a and Supplementary Fig. 3). In addition, the costs for C_2H_4 production through the proposed ESAE process decrease rapidly along with the increase in current densities and FE of C_2H_4 (Supplementary Fig. 4 and Supplementary Note 2). As a result, a ≥ 85% FE of C_2H_4 under industrially relevant current densities (≥ 0.2 A cm^{-2}) is determined as a basic target for the electrocatalytic semihydrogenation of acetylene to ethylene.

To design a suitable electrode with relatively high ethylene FE and yield, three factors should be considered: (1) low activation energy for water dissociation and small Gibbs free energy (ΔG_{H*}) for H^* formation[33,34]; (2) high energy barriers for H^* coupling to suppress competitive HER; and (3) easy desorption of ethylene to avoid overhydrogenation and C-C coupling[35,36]. First, DFT calculations are conducted to evaluate Cu materials. Periodic Cu slabs were used as the model of bulk Cu, and Cu clusters were represented for nanosized Cu with rich unsaturated sites for comparison because the size could alter the hydrogen-involved behavior of Cu catalysts in the thermocatalytic process (Supplementary Note 3 and Supplementary Table 2). The energy barrier for H_2O activation and cleavage over nanosized Cu is lower than that of bulk Cu (1.39 vs. 1.67 eV) (Fig. 1b and Supplementary Figs. 5, 6 and Supplementary Notes 4, 5), demonstrating the better H_2O dissociation ability over nanosized Cu. In addition, the formation of H^* over nanosized Cu is exothermic, while it is endothermic over bulk Cu, suggesting the more favorable formation of H^* over nanosized Cu. The H^* coupling barrier over nanosized Cu is larger than the corresponding bulk Cu under different coverage of H* (Supplementary Fig. 7 and Supplementary Note 6), indicating that nanosized Cu can hinder the competitive HER. Moreover, a lower energy is required for the desorption of the adsorbed ethylene over nanosized Cu (Supplementary Fig. 8 and Supplementary Note 7), thus preventing the overhydrogenation of C_2H_4 to C_2H_6. Furthermore, the energy change profiles of transition states during the coupling process show that both the relaxation steps and coupling barrier of nanosized Cu are higher than those of the bulk Cu counterpart, indicating that C–C coupling for C_{4+} production can be effectively avoided over nanosized Cu (Supplementary Fig. 9 and Supplementary Note 8). These calculated results reveal that nanosized Cu with rich unsaturated sites can not only promote H^* formation but also suppress competitive HER and acetylene overhydrogenation, thus accelerating ethylene production.

Electrocatalyst Synthesis And Characterizations

The abovementioned nanosized Cu with rich unsaturated sites was designedly synthesized on GDL-CP through a facile electrodeposition strategy (Fig. 2a). To avoid the formation of large Cu particles in typical

electrodeposition (Supplementary Fig. 10 and Supplementary Note 9), the slow dissolution of copper nitrate on the hydrophobic surface of GDL-CP causes the gradual release of Cu cations to form $Cu(OH)_2$, which acts as the in situ Cu source for electrodeposition preparation of low-coordination Cu nanoparticles (ED-Cu NPs). The formation process of ED-Cu NPs was monitored by in situ potential-dependent X-ray diffraction (XRD) (Fig. 2b). The peak at 54.5° is one of the characteristic peaks of CP (JCPDS No. 26–1076)[33,37]. The XRD peaks that appear in the initial sample immersed in aqueous KOH without electricity are ascribed to $Cu(OH)_2$, which is consistent with the results of the Raman spectra discussed later, affirming the existence of $Cu(OH)_2$ intermediates. (Supplementary Fig. 11 and Supplementary Note 10)[38]. Two characteristic peaks at 43.3° and 50.6° corresponding to the (111) and (200) crystal facets of cubic Cu[39] appear at approximately − 0.4 V vs. reverse hydrogen electrode (RHE), in line with the reduction peak of copper nitrate in the linear sweep voltammetry (LSV) curves and the Pourbaix diagram of the Cu-O system (Supplementary Fig. 12 and Supplementary Note 11)[40]. The two peaks become stronger with a potential negative shift. Thus, the results of in situ potential-dependent XRD patterns suggest that copper nitrate can completely transform into metallic Cu during the electrodeposition process. Then, the electrodeposition process was also confirmed by time-dependent electrochemical Raman spectroscopy. The intensities of peaks located at 294 and 497 cm^{-1} corresponding to $Cu(OH)_2$ decrease gradually and disappear with increasing time at − 0.35 V vs. RHE (Supplementary Fig. 13 and Supplementary Note 12), suggesting the complete conversion of the copper precursor and the formation of ED-Cu NPs because of the absence of characteristic peaks of metallic Cu(0) species[39,41]. Moreover, X-ray absorption spectroscopy (XAS) was used to further validate the electronic configuration and local coordination environment of the ED-Cu NPs. The Cu *K*-edge X-ray absorption near-edge structure spectra (XANES) of ED-Cu NPs exhibit similar features to Cu foil (Fig. 2c), agreeing with the in situ XRD results. In addition, the continuous Cauchy wavelet transform (WT) was applied to the extended X-ray absorption fine structure (EXAFS) spectra (Fig. 2d). The similar spectra of ED-Cu NPs and Cu foil further indicate that the parent copper nitrate is completely converted into metallic Cu. The local coordination environment of the as-obtained ED-Cu NPs is analyzed by the corresponding k^3-weighted Fourier transformed EXAFS curves (Fig. 2e). The Cu-Cu bonds with a bond length of 2.3 Å and Cu-O bonds with a bond length of 1.5 Å of the ED-Cu NPs are consistent with Cu foil[39,42]. However, in comparison with Cu foil, the increased coordination number of the Cu-O bond and the reduced coordination number of the Cu-Cu bond of ED-Cu NPs further illustrate that the ED-Cu NPs are more sensitive to oxygen in air than the bulk Cu, ascribed to the unsaturated site in the low-coordination Cu. The high-resolution transmission electron microscopy (HRTEM) images (Fig. 2f) show that the fringe spacing of 0.208 nm matches well with the (111) lattice plane of Cu, confirming the metallic nature of the ED-Cu NPs. The high-angle annular dark-field (HAADF) image, the associated scanning transmission electron microscope EDS (STEM-EDS) element mapping images (Fig. 2g, h), and the corresponding size distribution (Supplementary Fig. 14 and Supplementary Note 13) suggest that the ED-Cu NPs with an average diameter of approximately 3–5 nm are highly dispersed on GDL-CP. All these results demonstrate the successful preparation of ED-Cu NPs with unsaturated Cu sites.

Electrocatalytic Semihydrogenation Of Acetylene To Ethylene

The electrocatalytic acetylene semihydrogenation performances over ED-Cu NPs and commercial Cu were evaluated in a three-electrode flow cell with a gas diffusion layer under galvanostatic conditions (Fig. 3a). The performance evaluations in acidic, neutral, and basic electrolytes suggest that the alkaline solution is preferable (Supplementary Fig. 15 and Supplementary Note 14). Thus, a 1 M KOH aqueous solution and pure C_2H_2 are chosen as the electrolyte and reaction gas, respectively (Supplementary Fig. 16). Interestingly, it can be seen from the LSV curves that there is a much lower onset potential and slightly higher current densities in the potential range from 0 V to − 1.0 V vs. RHE over ED-Cu NPs than those of commercial Cu under an Ar atmosphere (Supplementary Fig. 17). The as-observed results suggest that H_2O activation proceeds more easily on nanosized Cu, agreeing with the prediction from the DFT calculation. Moreover, ED-Cu NPs exhibit smaller current densities at potentials more negative than − 1.0 V vs. RHE than commercial Cu (Supplementary Fig. 17 and Supplementary Note 15) because of their higher energy barriers in H^* self-coupling to form H_2 gas. In addition, a noticeable increase in current density can be observed when Ar is switched to C_2H_2 from the LSV curves (Supplementary Fig. 18 and Supplementary Note 16), suggesting that C_2H_2 can be activated over metallic Cu. The ESAE is analyzed in the current density range from 0.1 to 1.0 A cm^{-2} (Figs. 3b, c). The FE of C_2H_4 reaches above ~ 90%, and the H_2 byproduct is almost undetectable in a wide range of current densities from 0.1–0.5 A cm^{-2} on ED-Cu NPs (Supplementary Fig. 19a and Supplementary Note 17), which are superior to most reported catalysts in both electrocatlytic and thermocatalytic semihydrogenation of acetylene (Supplementary Fig. 20 and Supplementary Tables 3, 4). However, the FE of C_2H_4 decreases rapidly with more H_2 and a small amount of overhydrogenated ethane (C_2H_6) produced at current densities higher than 0.2 A cm^{-2} over commercial Cu (Supplementary Fig. 19b). In addition, the obtained C_2H_4 production rate of ED-Cu NPs at a current density of 0.5 A cm^{-2} is 70.15 mmol mg^{-1} h^{-1}, greatly surpassing the 13.44 mmol mg^{-1} h^{-1} over the commercial Cu counterpart (Supplementary Figs. 21, 22). Furthermore, the ED-Cu NPs also exhibit much higher performance than Cu macroparticles (Supplementary Fig. 23 and Supplementary Note 18), supporting the importance of the nanosized particles in our method. Considering the demands for industrial production, the current density should be increased as much as possible on the premise of relatively high FE and selectivity of the target C_2H_4. According to the TEA results in Supplementary Fig. 3, it is profitable when the FE of C_2H_4 is above 70% at 0.4 A cm^{-2}. Impressively, the FE of C_2H_4 over ED-Cu NPs is higher than 98% at 0.4 A cm^{-2}, and 85% at 1.0 A cm^{-2} (Fig. 3b), which are within the profitable region. Thus, these results indicate that the ED-Cu NPs are superior to commercial Cu from the aspect of both C_2H_4 yield and economic potential through ESAE.

To avoid the interference of the electrochical active surface (ECSA) on the catalytic performance, we compared their ECSA-normalized data. The FEs of C_2H_4 over ED-Cu NPs are still higher than the corresponding commercial Cu counterpart under the ECSA-normalized current densities (Supplementary Figs. 24, 25, and Supplementary Notes 19), indicating the remarkable HER suppression ability of the designed ED-Cu NPs. Moreover, the ECSA-normalized performance (Supplementary Figs. 26 and

Supplementary Notes 20) shows that ED-Cu NPs exhibit higher normalized partial current densities and larger turnover frequency (TOF) values of C_2H_4 than their commercial counterpart, highlighting the high intrinsic activity of ED-Cu NPs. Furthermore, the performance and size distribution comparison of ED-Cu NPs with different loadings of Cu precursor suggests that the ultrasmall particle with a size of < 5 nm is critical to achieving high C_2H_4 selectivity and FE under high current densities (Supplementary Fig. 27 and Supplementary Note 21), further affirming the role of HER suppression of the ultrasmall Cu nanoparticles. To clarify the selectivity issues during the ESAE process more clearly, online differential electrochemical mass spectrometry (DEMS) was conducted using a scanning flow cell (SFC) (Figs. 3d, e, Supplementary Figs. 28, 29, and Supplementary Note 22). Although C_2H_4 is formed at a current density of 0.1 A cm^{-2} over both ED-Cu NPs and commercial Cu, the H_2 emerges above 0.4 A cm^{-2} over ED-Cu NPs, much later than the 0.2 A cm^{-2} over commercial Cu, further indicating the better C_2H_4 selectivity of ED-Cu NPs under industrially relevant current density. The signal of C_2H_6 with a relatively low intensity can only be observed over commercial Cu, agreeing with the detected overhydrogenated C_2H_6 (Fig. 3c). Furthermore, both the FE of C_2H_4 and the conversion of C_2H_2 over ED-Cu NPs remain unchanged within the error range during the 54 h continuous test at a current density of 0.2 A cm^{-2}, suggesting robust durability (Fig. 3f and Supplementary Figs. 30a-d). To make the ESAE compatible with the intermittent and variable characteristics of renewable energy sources (e.g., solar, and wind energy), step hydrogenation stability evaluation experiments were performed (Supplementary Figs. 30e, f and Supplementary Note 23). The FE of C_2H_4 and the conversion of C_2H_2 over ED-Cu NPs keep unchanged at different potentials (from − 1.0 to − 1.4 to − 1.0 V vs. RHE) or different current densities (from 0.1 to 0.3 to 0.1 A cm^{-2}), indicating that the proposed catalysts exhibited potential- and current density-independent ESAE activity. Thus, our low-cost catalyst can operate under fluctuant renewable energy sources, which is highly challenging for other catalysts. The additional experiment shows that the as-proposed ESAE process can also be driven by the electricity generated from renewable solar energy (Supplementary Movie 1), further highlighting the potential of our strategy as a sustainable alternative/complementary to the traditional petroleum route for C_2H_4 production.

Mechanistic Insight Into The High Selectivity For Ethylene

To elucidate the reaction pathway of the ESAE process, a series of in situ and *ex situ* characterizations were performed. First, in situ Raman spectra were carried out to investigate the reaction intermediates during the ESAE process in the potential range of − 0.6 to − 1.2 V vs. RHE, within the corresponding potential range in the performance evaluation under galvanostatic conditions (Supplementary Fig. 31). The peaks located at 1700 cm^{-1} and 1560 cm^{-1} in Fig. 4a are assigned to the $^*C \equiv C$ bond of C_2H_2 and the generated $^*C = C$ bond[14,17,18] adsorbed on ED-Cu NPs in C_2H_2-saturated solution, respectively. The intensity of $^*C_2H_2$ decreases while the intensity of $^*C = C$ increases rapidly as the electrode potential becomes more negative, suggesting that the original C_2H_2 is hydrogenated to $^*C_2H_4$. Moreover, in situ attenuated total reflectance-Fourier transform infrared (ATR-FTIR) spectroscopy, which is highly sensitive

to intermediates, was further conducted to probe the mechanism of the ESAE process. As shown in Fig. 4b, the $^*C_2H_2$ adsorbed species can also be detected at 1641 cm^{-1} over ED-Cu NPs. The peak located at 1577 cm^{-1} is attributed to $^*C_2H_3$, the reaction intermediate of C_2H_2 hydrogenation[17,43]. Moreover, apart from the $^*C_2H_2$ and $^*C_2H_3$ species, the vibrations of the C-H bond in alkanes (2924 cm^{-1}) can only be detected over the commercial Cu electrode (Supplementary Fig. 32 and Supplementary Note 24)[44,45], further confirming the overhydrogenation phenomenon of commercial Cu. To further clarify the hydrogenation pathway, quasi-in situ electron paramagnetic resonance (EPR) was adopted to analyze the radicals adsorbed on the electrode during the ESAE process. No signals can be detected under the open circuit potential (OCP), whereas strong signals assigned to carbon and hydrogen radicals emerge rapidly under a current density of 50 mA cm^{-2} over both ED-Cu NPs and commercial Cu (Fig. 4c, Supplementary Fig. 33, and Supplementary Note 25, 26)[33]. The extremely low concentration of protons in our alkaline electrolytes does not favor the proton-coupled electron transfer process. Thus, a H^* addition transfer hydrogenation pathway is rationally proposed in the ESAE process. Namely, H^* formed by H_2O dissociation is first transferred to $^*C_2H_2$, which is activated and adsorbed on the surface of the ED-Cu electrode to generate $^*C_2H_3$. Subsequently, another H^* is further coupled with $^*C_2H_3$ to produce the target C_2H_4.

Generally, H_2O dissociation and C_2H_2 hydrogenation are involved during the ESAE process. To further understand the enhanced production of C_2H_4 over ED-Cu NPs, we further explored the reaction mechanism by DFT calculations, the kinetic isotope effect (KIE), and controlled experiments. The DFT calculation results show that ED-Cu NPs exhibit a higher energy barrier for H^* self-coupling than that for the $^*C_2H_2$ hydrogenation process compared with commercial Cu (Fig. 4d and Supplementary Figs. 34–37 and Supplementary Note 27). These DFT comparison results indicate that sufficient hydrogen radicals adsorbed on electrodes are more likely to participate in the $^*C_2H_2$ hydrogenation process, rather than self-coupling to generate H_2 over ED-Cu NPs. Moreover, the KIE experiment was carried out between the same potential range with performance evaluation and in situ characterization. As shown in Supplementary Fig. 38, the k_H/k_D values among the four selected potentials are all larger than 2, indicating that the O-H cleavage of the H_2O dissociation part is the rate-determining step of the whole EASE process[33,39]. This rate-determining step is also supported by the difference in the energy barriers of the H_2O dissociation and C_2H_2 hydrogenation processes (Figs. 1b and 4d), indicating the importance of H^* formation and reserves in the ESAE process. Consequently, the cyclic voltammogram (CV) curve in 1 M KOH solution was conducted to confirm the behavior of H^*. The distinctly larger peak of H^* suggests the existence of abundant H^* and the relatively stronger H^* adsorption ability of ED-Cu NPs[35,46] (Supplementary Fig. 39 and Supplementary Note 28), further affirming the DFT calculation results of H_2O activation (Fig. 1b). Accordingly, a schematic illustration of the whole reaction route is given in Supplementary Fig. 40, and the in-depth origins for the enhanced C_2H_4 selectivity at industrially relevant current density are summarized in Fig. 4e. On the one hand, the increased H_2O activation and dissociation ability enable

enough H^* to participate in the subsequent H^* addition transfer hydrogenation process. On the other hand, the higher energy barrier of H^* coupling and the easier desorption of C_2H_4 hinders the competitive HER and undesired overgydrogenation and further guarantees the progress of the transfer hydrogenation process to efficiently produce C_2H_4.

Discussion

To confirm the economic potential of the proposed ESAE process in C_2H_4 production as an alternative/complementary for the petroleum or shale gas route, the subdivided costs of the entire technological process consisting of the arc pyrolysis process of coal and electrocatalytic C_2H_2 semihydrogenation are proposed in Fig. 5a and Supplementary Table 5. The electricity cost accounts for the highest proportion, which can be conquered soon with the development of renewable electricity generation technology. In addition, the total costs of separation equipment and operation are as high as 17.6%, the second largest cost. In this regard, developing an efficient catalyst to suppress undesired H_2 at high current densities to lower the separation cost is of great significance. Therefore, the electrosynthesis of C_2H_4 through electrochemical semihydrogenation of coal-derived C_2H_2 with high selectivity and FEs possesses huge economic potential. Moreover, an LCA on CO_2 emissions from cradle-to-gate was conducted to prove the environmentally friendly potential of the proposed ESAE strategy (Supplementary Note 29)[47]. The amount of CO_2 emissions per kilogram of C_2H_4 as a function of electricity carbon intensity is shown in Fig. 5b. The CO_2 emission amount of the coal-derived strategy is much higher than that of the petroleum route (3.2 $kgCO_2/kgC_2H_4$) using electricity from the traditional thermal power plant (Supplementary Tables 6, 7). However, a breakeven appears when the carbon intensity of the electricity is lower than 73 g CO_2-e per kWh. Fortunately, the carbon intensity of renewable electricity such as solar and wind power generation could meet the standard according to the state-of-the-art report and technology[48]. In addition, the CO_2 emission of our proposed ESAE process is expected to be further reduced by increasing the energy efficiency by lowering the cell voltage (Supplementary Fig. 41 and Supplementary Note 30). Thus, the abovementioned results indicate that the proposed ESAE process of coal-derived acetylene deserves to be developed from the aspects of both the economy and the environment.

In summary, the results of TEA demonstrate the ESAE process as an efficient alternative/complementary method to produce C_2H_4 at an industrially relevant current density ($\geq$ 0.2 A cm^{-2}) with tremendous economic potential. The DFT calculations show that low-coordination nanosized Cu is a promising candidate for inhibiting the competing HER due to the high energy barrier for H^* coupling to release H_2, leading to higher C_2H_4 production. Thus, low-coordination ED-Cu NPs with a size of 3–5 nm are designedly synthesized and proven to be an efficient cathode for C_2H_4 production under 0.5 A cm^{-2} with a 97.7% FE and 70.15 mmol mg^{-1} h^{-1} production rate through the ESAE process, greatly outperforming the commercial Cu counterpart (13.44 mmol mg^{-1} h^{-1}) and electrodeposited Cu macrosized particles (12.37 mmol mg^{-1} h^{-1}). Moreover, an H^* addition mechanism is proposed for C_2H_4 formation by a series

of in situ spectroscopic characterizations. Furthermore, KIE and DFT results suggest that sufficient H^* on ED-Cu enables a high C_2H_4 FE in a wide current density window. Furthermore, our strategy is a potential alternative/complementary to the petroleum route, which is proven by cradle-to-gate LCA. Impressively, the FE of C_2H_4 and the conversion of C_2H_2 over ED-Cu NPs can remain unchanged over a wide range of potentials or current densities. Thus, the process can operate under fluctuant renewable energy sources, which is highly challenging for other catalysts, further highlighting the promising potential of our strategy. Our work may not only establish a green and sustainable electrocatalytic complementary strategy for continuous C_2H_4 production with high yield and selectivity but also offer a paradigm for designing nanocatalysts to inhibit the competitive HER during electrocatalytic transfer hydrogenation using water as the hydrogen source.

Methods

Chemicals. Copper nitrides ($Cu(NO_3)_2$), potassium hydroxide (KOH), and 5,5-dimethyl-1-pyrroline-N-oxide (DMPO) were purchased from Aladdin Ltd. (Shanghai, China). Ar and pure C_2H_2 gas were purchased from Taiya (Tianjin) Co., Ltd. Gas diffusion layer-coated carbon paper (GDL-CP) was purchased from Gaossunion Co., Ltd. (Tianjin, China). Deionized water (DIW) was used in all the experimental processes. All chemicals were of analytical grade and used without further purification.

Fabrication of GDL-CP-supported copper nitrate (GDL-CP $Cu(NO_3)_2$) electrodes. GDL-CP $Cu(NO_3)_2$ electrodes were fabricated by the traditional spin-casting method according to a previous report with a slight modification. The commercial GDL-CP was cut into a rectangular shape with a size of 1.2 × 3.3 cm^2 as the electrode substrate. Specifically, $Cu(NO_3)_2$ was dissolved in a mixed solvent of water and ethanol with a volume ratio of 1/3 to form a solution at a concentration of 2 mg mL^{-1}. Then, the as-prepared solution was spin-coated on the GDL-CP substrates with 1 mL on each substrate under a constant spin speed of 500 rpm.

Synthesis of GDL-CP-supported Cu nanoparticles. The electrodeposition of GDL-CP $Cu(NO_3)_2$ was performed in the flow cell reactor using an electrochemical workstation (CS150H, CorrTest, Wuhan). The electrolyte and reference electrode were 1 M KOH and Hg/HgO electrode with 1.0 M KOH as the inner reference electrolyte, respectively. A platinum (Pt) foil was used as the counter electrode. Note that the apparatus conditions are all the same as those for performance evaluation, except the atmosphere is Ar rather than C_2H_2. The as-prepared GDL-CP $Cu(NO_3)_2$ electrode was fixed with conductive copper tape and used as the working electrode. The continuous LSV measurement was conducted in the voltage range of 0 ~ − 1.5 V vs. RHE at a scan rate of 5 mV s^{-1} until the reductive peak disappeared.

Synthesis of GDL-CP-supported Cu microparticles. The electrodeposition method was carried out in a typical H-cell electrolytic tank according to the previous literature[49]. First, the deposition solution consisted of 0.4 M $Cu(NO_3)_2$ and 3 M lactic acid, and the pH value was adjusted to 11.5 using NaOH powder. A Ag/AgCl electrode with saturated KCl as the inner reference electrolyte and a platinum (Pt) foil

were used as the reference and counter electrodes. Then, the as-prepared solution was preheated in a 60°C water bath, and electrodeposition was performed under − 0.4 V vs. RHE, and the deposition amount was controlled by adjusting the Coulombs passed through the electrodeposition process.

Characterization. Ex situ and in situ X-ray diffraction (XRD) was performed on a Bruker D8 Focus Diffraction System (Germany) using a Cu *K*α source (λ = 0.154178 nm) and a Rigaku Smartlab9KW Diffraction System using a Cu *Kα* source (λ = 0.15406 nm), respectively. Transmission electron microscopy (TEM) images were obtained with a JEOL-2100F system equipped with EDAX Genesis XM2. The operando online SFC/DEMS analysis was conducted by QAS 100 provided by Linglu instruments (Shanghai) Co. Ltd. The in situ ATR-FTIR was performed on a Nicolet 6700 FTIR spectrometer with silicon as the prismatic window. The in situ Raman spectroscopy was acquired on a Renishaw inVia reflex Raman microscope under the excitation of a 532 nm laser. The X-ray absorption spectroscopy (XAS) measurements were undertaken at the 1W1B beamline of the BSRF. The XAS spectra were analysed with the ATHENA software package. The gas chromatograph (GC) was measured on a Shimadzu GC-2010 Plus with a ShinCarbon ST100/120 column and Barrier Discharge Ionization Detector (BID). Helium (He) was used as the carrier gas. The injection temperature was set at 240°C.

Electrochemical measurements in the flow cell. Electrochemical measurements were carried out in a typical flow cell consisting of a GDL as the working electrode, a Pt foil as the counter electrode, and Hg/HgO as the reference electrode using a CS150H electrochemical workstation. The cathode cell and anode cell are separated by a Nafion 117 proton exchange membrane. The cathode and anode electrolytes are both 1.0 M KOH solution, and a peristaltic pump was applied to implement the circulation of the liquid phase. The gas flow rate was controlled by the mass flowmeter. A schematic illustration of the flow cell is shown in Fig. 3a. Before the performance tests, the working electrode was fixed at the interface between the gas flow block and the cathodic electrolyte block by conductive copper tape. First, the in situ electrodeposition of GDL-CP $Cu(NO_3)_2$ through a series of negative direction LSV processes was carried out under an Ar atmosphere at a flow rate of 30 mL min^{-1}. Then, after the ED-Cu NPs were formed in situ, the Ar gas was switched to pure C_2H_2 gas with the flow rate maintained at 30 mL min^{-1}. The electrochemical semihydrogenation of acetylene was conducted at different current densities for 10–20 min to achieve relatively stable and reliable performance parameters before the quantitative analysis. The gas at the flow cell outlet was directly introduced into the gas chromatograph for the analysis of the products. The procedure and reaction setup of electrochemical semihydrogenation of acetylene over commercial Cu was similar to that of ED-Cu NPs except that the in situ electrodeposition process for the working electrode was excluded. All LSV curves were *iR* compensated with a compensation level of 80%. For Tafel slopes, the LSV curves were replotted by using the logarithms of current density as the x-axis and potential as the y-axis. Then, the obtained slopes of the linear part of the replotted figure were Tafel slopes.

The quantitative analysis of the C_2H_2 conversion, as well as the evolution rate, FE, and turnover frequency (TOF) of the obtained products. The products were subjected to the GC-2010 gas chromatograph

equipped with an activated carbon packed column (He as carrier gas) and barrier discharge ionization detector. The calculation of the C_2H_2 conversion and evolution rate of different products was performed using equations (1) and (2), and the FEs of different products were calculated using Eq. (3). TOF for C_2H_4 was calculated using Eq. (4). All experiments were repeated three times.

$$\text{Conversion } (\%) = \frac{\text{the peak area of B-peak area of A}}{\text{the peak area of B}} \times 100\% \ (1)$$

$$\text{Evolution Rate } (\text{mmol/mg/h}) = \frac{\text{the peak area of X} \times \text{C}}{\text{the peak area of standard gas} \times \text{m}} \times \text{S} \ \ (2)$$

$$\text{FE}_\text{X} \ (\%) = \frac{\text{a} \times \text{n}_\text{X} \times \text{F}}{\text{Q}} (3)$$

$$\text{TOF } (\text{min}^{-1}) = \frac{\text{The amount of produced } C_2H_4 \text{ molecules per min}}{\text{The amount of Cu sites}} \ (4)$$

X: The different products, including H_2, C_2H_4, and C_2H_6.
C: The concentration of X in standard gas.

m: The mass of metallic Cu over the electrode.

n: The moles of different products, including H_2, C_2H_4, and C_2H_6.

A: The area of the C_2H_2 outlet; B: The area of the C_2H_2 inlet.

S: The gas flow rate.

a: Electron transfer number.

F: Faraday constant.

Q: The total Coulomb number of the ESAE process.

Electrochemical in situ XRD measurements

The in situ electrochemical XRD patterns were measured with a Rigaku Smartlab9KW Diffraction System using a Cu *K*α source (λ = 0.15406 nm). The electrolytic cell used in the in situ XRD measurement was homemade by Teflon. The Pt wire and Hg/HgO electrode were used as the counter and reference electrodes, respectively. Diffraction patterns were recorded within a 2θ range of 30–80° under the applied potential from OCP to − 0.7 V vs. RHE. The scanning rate was 10°/min.

Electrochemical in situ Raman spectra measurements

The in situ electrochemical Raman spectroscopy was recorded on a Renishaw inVia reflex Raman microscope under an excitation of 532 nm laser under controlled potentials by an electrochemical

workstation. We used a homemade Teflon electrolytic cell equipped with a piece of round quartz glass for the incident laser and the protection of the tested samples. Before the experiments, the electrolyte was pretreated with pure C_2H_2 gas to obtain C_2H_2-saturated KOH. The working electrode was parallel to the quartz glass to keep the plane of the sample perpendicular to the incident laser. Pt wire was rolled to a circle around the working electrode to serve as the counter electrode. The reference electrode was Hg/HgO with an internal reference electrolyte of 1.0 M KOH. The spectrum was recorded under an applied potential of − 0.35 V vs. RHE and every 30 s under the applied potential from OCP to − 1.2 V vs. RHE, respectively.

Electrochemical in situ ATR-FTIR spectra measurements

The *in situ* ATR-FTIR was performed on a Nicolet 6700 FTIR spectrometer equipped with an MCTA detector with silicon as the prismatic window and an ECIR-II cell by Linglu instruments. First, $Cu(NO_3)_2$ ink was carefully dropped on the surface of the gold film, which was chemically deposited on the surface of the silicon prismatic before each experiment. Then, the deposited silicon prismatic served as the working electrode. The Pt foil and Hg/HgO with an internal reference electrolyte of 1.0 M KOH were used as the counter and reference electrodes, respectively. A 1 M KOH solution was employed as the electrolyte. The electrolyte was presaturated with pure C_2H_2 gas, and the gas was continuously bubbled during the whole measurement. Before spectral acquisition, the working electrode was pretreated through a series of continuous LSV measurements in the voltage range of 0 ~ − 1.5 V vs. RHE for the *in situ* formation of ED-Cu NPs. The spectrum was recorded every 30 s under the applied potential from OCP to − 1.2 V vs. RHE.

Electrochemical operando online SFC/DEMS analysis

The operando online SFC/DEMS analysis was conducted by QAS 100 provided by Linglu instruments (Shanghai) Co. Ltd. Because the products in the proposed ESAE process are all in the gas phase, *operando* experiments were conducted to monitor the distribution of the products during the reaction on-stream, clarifying the selectivity issues more directly and clearly. The flow cell used in performance evaluation and the DEMS were coupled to ensure that the gas at the flow cell outlet was directly injected into the negatively pressured gas circuit system of the DEMS through a quartz capillary that was inserted into the outlet of the flow cell. The rectangular wave current density was applied from 0.1 to 0.5 A cm^{-2} with a constant interval of 400 s by the CS150H electrochemical workstation. During the experiment, the flow rate of C_2H_2 gas and electrolyte was set the same as the performance evaluation.

Computational details. In this work, all DFT calculations were performed using the Vienna Ab initio Simulation Package (VASP)[50]. The projector augmented wave (PAW) pseudopotential[51] with the PBE generalized gradient approximation (GGA) exchange correlation function[52] was utilized in the computations. The cut-off energy of the plane wave basis set was 500 eV, and a Monkhorst-Pack mesh of 3×3×1 was used in K-sampling in the adsorption energy calculation. The long-range dispersion interaction was described by the DFT-D3 method. The electrolyte was incorporated implicitly with the Poisson-Boltzmann model implemented in VASPsol[53]. The relative permittivity of the media was chosen

as ϵ_r = 78.4, corresponding to that of water. The Debye length for the electrolyte was set to 3.0 Å, which corresponds to an electrolyte concentration of 1.0 M. All atoms were fully relaxed with an energy convergence tolerance of 10^{-5} eV per atom, and the final force on each atom was < 0.01 eV $Å^{-1}$. The transition state (TS) searches are performed using the Dimer method in the VTST package. The final force on each atom was < 0.05 eV $Å^{-1}$. The TS search is conducted by using the climbing-image nudged elastic band (CI-NEB) method to generate initial guess geometries, followed by the dimer method to converge to the saddle points.

In this work, face-centered cubic (fcc) phase copper (Cu) is used ($a = b = c = 3.621$ Å, $\alpha = \beta = \gamma = 90.0°$, Fm-3 m). The bulk model of the sample was built by the 3×3 supercell of Cu (111) with four layers of Cu. All periodic slabs have a vacuum layer of at least 15 Å. The bottom layer of atoms is fixed at their optimized bulk-truncated positions during geometry optimization, and the rest of the atoms can relax. The model of the nanosized sample was built by a cluster of 38 Cu atoms in a 20 Å×20 Å×25 Å unit cell, and all the atoms could relax.

The adsorption energy of reaction intermediates and reaction free energy change can be obtained with the following equations (4)-(5):

$$\Delta E_{ads} = E_{(ads/slab)} - E_{ads} - E_{slab} \quad (4)$$

$$\Delta G = \Delta E + \Delta E_{ZPE} - T\Delta S \quad (5)$$

where ΔE is the total energy difference between the products and the reactants of each reaction step and ΔE_{ZPE} and ΔS are the differences in zero-point energy and entropy, respectively.

The energy of the reaction can be calculated by Equations (6)-(12):

$$*+C_2H_2 — — *C_2H_2 \quad (6)$$

$$*C_2H_2 + H^+ + e^- — — *C_2H_2 + *H \quad (7)$$

$$*C_2H_2 + *H + H^+ + e^- — — *C_2H_2 + 2*H \quad (8)$$

$$*C_2H_2 + 2*H — — *C_2H_3 + *H \quad (9)$$

$$*C_2H_3 + *H — — *C_2H_4 \quad (10)$$

$$*C_2H_4 — — * + C_2H_4 \quad (11)$$

$$*H + *H — — * + H_2 \quad (12)$$

Declarations

Data availability

The source data underlying Figs. 1–5 are provided as Source Data files 1-5 with this paper. The spreadsheets used for cost analyses and CO_2 emissions and supplementary Tables S1-S7 are available in Supplementary datasets 1-2.

Acknowledgements

We acknowledge the National Natural Science Foundation of China (No. 21871206 to B. Z.) and Dr. Lirong Zheng at the 1W1B beamline of the Beijing Synchrotron Radiation Facility for supporting this project. We also appreciate the kind help from Ms. Yang Liu for ATR-FTIR measurements.

Author Contributions

B.Z. conceived the idea and directed the project. B.H.Z and B.Z designed the experiments. B.H.Z. and M.W. performed the materials synthesis and electrochemical experiments. B.H.Z., F.C., and M.W. carried out the in situ experiments. C.C. performed and analyzed the DFT calculations. B.H.Z., Y.W., C.L., Y.Y. and B.Z. analyzed experimental data. B.H.Z and F.C. wrote the paper. B.Z. revised the paper. All authors discussed the results and commented on the paper.

Competing interests

The authors declare no competing interests.

References

1. Leow, W. R. et al. Chloride-mediated selective electrosynthesis of ethylene and propylene oxides at high current density. *Science* **368**, 1228-1233 (2020).
2. Jiang, K. et al. Metal ion cycling of Cu foil for selective C–C coupling in electrochemical CO_2 reduction. *Nat. Catal.* **1**, 111-119 (2018).
3. Chai, Y. et al. Control of zeolite pore interior for chemoselective alkyne/olefin separations. *Science* **368**, 1002-1006 (2020).
4. Bodke, A. S., Olschki, D. A., Schmidt, L. D. & Ranzi, E. High selectivities to ethylene by partial oxidation of ethane. *Science* **285**, 712-715 (1999).
5. Gomez, E., Yan, B., Kattel, S. & Chen, J. G. Carbon dioxide reduction in tandem with light-alkane dehydrogenation. *Nat. Rev. Chem.* **3**, 638-649 (2019).
6. Gao, Y. et al. Recent advances in intensified ethylene production—A review. *ACS Catal.* **9**, 8592-8621 (2019).
7. Zhao, B. et al. Unveiling the activity origin of iron nitride as catalytic material for efficient hydrogenation of CO_2 to C_{2+} hydrocarbons. *Angew. Chem. Int. Ed.* **60**, 4496-4500 (2021).
8. Jiang, W. et al. Pd-modified ZnO–Au enabling alkoxy intermediates formation and dehydrogenation for photocatalytic conversion of methane to ethylene. *J. Am. Chem. Soc.* **143**, 269-278 (2021).

9. Jiao, X. et al. Conversion of waste plastics into value-added carbonaceous fuels under mild conditions. *Adv. Mater.* **33**, 2005192 (2021).
10. Schobert, H. Production of acetylene and acetylene-based chemicals from coal. *Chem. Rev.* **114**, 1743-1760 (2014).
11. Ma, J. et al. Pyrolysis of pulverized coal to acetylene in magnetically rotating hydrogen plasma reactor. *Fuel Process. Technol.* **167**, 721-729 (2017).
12. Bond, R. L., Galbraith, I. F., Ladner, W. R. & McConnell, G. I. T. Production of acetylene from coal, using a plasma jet. *Nature* **200**, 1313-1314 (1963).
13. Yan, B., Xu, P., Guo, C. Y., Jin, Y. & Cheng, Y. Experimental study on coal pyrolysis to acetylene in thermal plasma reactors. *Chem. Eng. J.* **207-208**, 109-116 (2012).
14. Zhang, L. et al. Efficient electrocatalytic acetylene semihydrogenation by electron-rich metal sites in N-heterocyclic carbene metal complexes. *Nat. Commun.* **12**, 6574 (2021).
15. Studt, F. et al. Identification of non-precious metal alloy catalysts for selective hydrogenation of acetylene. *Science* **320**, 1320-1322 (2008).
16. Cao, Y. et al. Adsorption site regulation to guide atomic design of Ni–Ga catalysts for acetylene semi-hydrogenation. *Angew. Chem., Int. Ed.* **132**, 11744-11749 (2020).
17. Wang, S. et al. Highly efficient ethylene production via electrocatalytic hydrogenation of acetylene under mild conditions. *Nat. Commun.* **12**, 7072 (2021).
18. Bu, J. et al. Selective electrocatalytic semihydrogenation of acetylene impurities for the production of polymer-grade ethylene. *Nat. Catal.* **4**, 557-564 (2021).
19. Shi, R. et al. Room-temperature electrochemical acetylene reduction to ethylene with high conversion and selectivity. *Nat. Catal.* **4**, 565-574 (2021).
20. Vilé, G., Albani, D., Almora-Barrios, N., López, N. & Pérez-Ramírez, J. Advances in the design of nanostructured catalysts for selective hydrogenation. *ChemCatChem* **8**, 21-33 (2016).
21. Vilé, G. et al. A stable single-site palladium catalyst for hydrogenations. *Angew. Chem., Int. Ed.* **54**, 11265-11269 (2015).
22. Omar, S. et al. Density functional theory analysis of dichloromethane and hydrogen interaction with Pd clusters: first step to simulate catalytic hydrodechlorination. *J. Phys. Chem. C* **115**, 14180-14192 (2011).
23. Huang, F. et al. Insight into the activity of atomically dispersed Cu catalysts for semihydrogenation of acetylene: impact of coordination environments. *ACS Catal.* **12**, 48-57 (2022).
24. Semagina, N. & Kiwi-Minsker, L. Recent advances in the liquid-phase synthesis of metal nanostructures with controlled shape and size for catalysis. *Catal. Rev.* **51**, 147-217 (2009).
25. Xing, Z., Hu, L., Ripatti, D. S., Hu, X. & Feng, X. Enhancing carbon dioxide gas-diffusion electrolysis by creating a hydrophobic catalyst microenvironment. *Nat. Commun.* **12**, 136 (2021).
26. Nguyen, T. N. & Dinh, C.-T. Gas diffusion electrode design for electrochemical carbon dioxide reduction. *Chem. Soc. Rev.* **49**, 7488-7504 (2020).

27. Yang, K., Kas, R., Smith, W. A. & Burdyny, T. Role of the carbon-based gas diffusion layer on flooding in a gas diffusion electrode cell for electrochemical CO_2 reduction. *ACS Energy Lett.* **6**, 33-40 (2021).
28. Gu, Y. et al. Two-dimensional porous molybdenum phosphide/nitride heterojunction nanosheets for pH-universal hydrogen evolution reaction. *Angew. Chem. Int. Ed.* **60**, 6673-6681 (2021).
29. Haase, F. T. et al. Size effects and active state formation of cobalt oxide nanoparticles during the oxygen evolution reaction. *Nat. Energy* **7**, 765-773 (2022).
30. Xie, L. et al. Molecular engineering of a 3D self-supported electrode for oxygen electrocatalysis in neutral media. *Angew. Chem., Int. Ed.* **58**, 18883-18887 (2019).
31. Lum, Y. et al. Tuning OH binding energy enables selective electrochemical oxidation of ethylene to ethylene glycol. *Nat. Catal.* **3**, 14-22 (2020).
32. Shin, H., Hansen, K. U. & Jiao, F. Techno-economic assessment of low-temperature carbon dioxide electrolysis. *Nat. Sustain.* **4**, 911-919 (2021).
33. Gao, Y. et al. Field-induced reagent concentration and sulfur adsorption enable efficient electrocatalytic semihydrogenation of alkynes. *Sci. Adv.* **8**, eabm9477 (2022).
34. Durante, C. An electrochemical way to pure ethylene. *Nat. Catal.* **4**, 537-538 (2021).
35. Wu, Y., Liu, C., Wang, C., Lu, S. & Zhang, B. Selective transfer semihydrogenation of alkynes with H_2O (D_2O) as the H (D) source over a Pd-P cathode. *Angew. Chem. Int. Ed.* **59**, 21170-21175 (2020).
36. Li, H. et al. σ-alkynyl adsorption enables electrocatalytic semihydrogenation of terminal alkynes with easy-reducible/passivated groups over amorphous PdS_x nanocapsules. *J. Am. Chem. Soc.* **144**, 19456-19465 (2022)
37. Higgins, D., Hahn, C., Xiang, C., Jaramillo, T. F. & Weber, A. Z. Gas-diffusion electrodes for carbon dioxide reduction: A new paradigm. *ACS Energy Lett.* **4**, 317-324 (2019).
38. Cheng, W., Zhang, H., Luan, D. & Lou, X. W. Exposing unsaturated Cu_1-O_2 sites in nanoscale Cu-MOF for efficient electrocatalytic hydrogen evolution. *Sci. Adv.* **7**, eabg2580 (2021).
39. Wu, Y. et al. Converting copper sulfide to copper with surface sulfur for electrocatalytic alkyne semi-hydrogenation with water. *Nat. Commun.* **12**, 3881 (2021).
40. Han, J. et al. A reconstructed porous copper surface promotes selectivity and efficiency toward C_2 products by electrocatalytic CO_2 reduction. *Chem. Sci.* **11**, 10698-10704 (2020).
41. Tao, Z., Wu, Z., Wu, Y. & Wang, H. Activating copper for electrocatalytic CO_2 reduction to formate via molecular interactions. *ACS Catal.* **10**, 9271-9275 (2020).
42. Lei, Q. et al. Investigating the origin of enhanced C_{2+} selectivity in oxide-/hydroxide-derived copper electrodes during CO_2 electroreduction. *J. Am. Chem. Soc.* **142**, 4213-4222 (2020).
43. Ma, C.Y. et al. Mesoporous Co_3O_4 and Au/Co_3O_4 catalysts for low-temperature oxidation of trace ethylene. *J. Am. Chem. Soc.* **132**, 2608-2613 (2010).
44. McKean, D. C. Individual CH bond strengths in simple organic compounds: effects of conformation and substitution. *Chem. Soc. Rev.* **7**, 399-422 (1978).

45. Yamamoto, M. et al. Softened CH stretching vibration of a long-chain n-alkane, n-$C_{44}H_{90}$, physisorbed on a Ag(111) surface: An infrared reflection absorption spectroscopic study. *J. Phys. Chem. B* **104**, 7370-7376 (2000).
46. Sherbo, R. S., Kurimoto, A., Brown, C. M. & Berlinguette, C. P. Efficient electrocatalytic hydrogenation with a palladium membrane reactor. *J. Am. Chem. Soc.* **141**, 7815-7821 (2019).
47. De Luna, P. et al. What would it take for renewably powered electrosynthesis to displace petrochemical processes? *Science* **364**, eaav3506 (2019).
48. Rojas Sánchez, D., Khalilpour, K. & Hoadley, A. F. A. How sustainable is CO_2 conversion to ethanol? — A life cycle assessment of a new electrocatalytic carbon utilisation process. *Sustain. Energy Fuels* **5**, 5866-5880 (2021).
49. Chang, X., Malkani, A., Yang, X. & Xu, B. Mechanistic insights into electroreductive C–C coupling between CO and acetaldehyde into multicarbon products. *J. Am. Chem. Soc.* **142**, 2975-2983 (2020).
50. Kresse, G. & Furthmüller, J. Efficient iterative schemes for ab initio total-energy calculations using a plane-wave basis set. *Phys. Rev. B* **54**, 11169 (1996).
51. Blöchl, P. E. Projector augmented-wave method. *Phys. Rev. B* **50**, 17953 (1994).
52. Perdew, J. P., Burke, K. & Ernzerhof, M. Generalized gradient approximation made simple. *Phys. Rev. Lett.* **77**, 3865 (1996).
53. Mathew, K., Sundararaman, R., Letchworth-Weaver, K., Arias, T. & Hennig, R.G. Implicit solvation model for density-functional study of nanocrystal surfaces and reaction pathways. *J. Chem. Phys.* **140**, 084106 (2014).

Figures

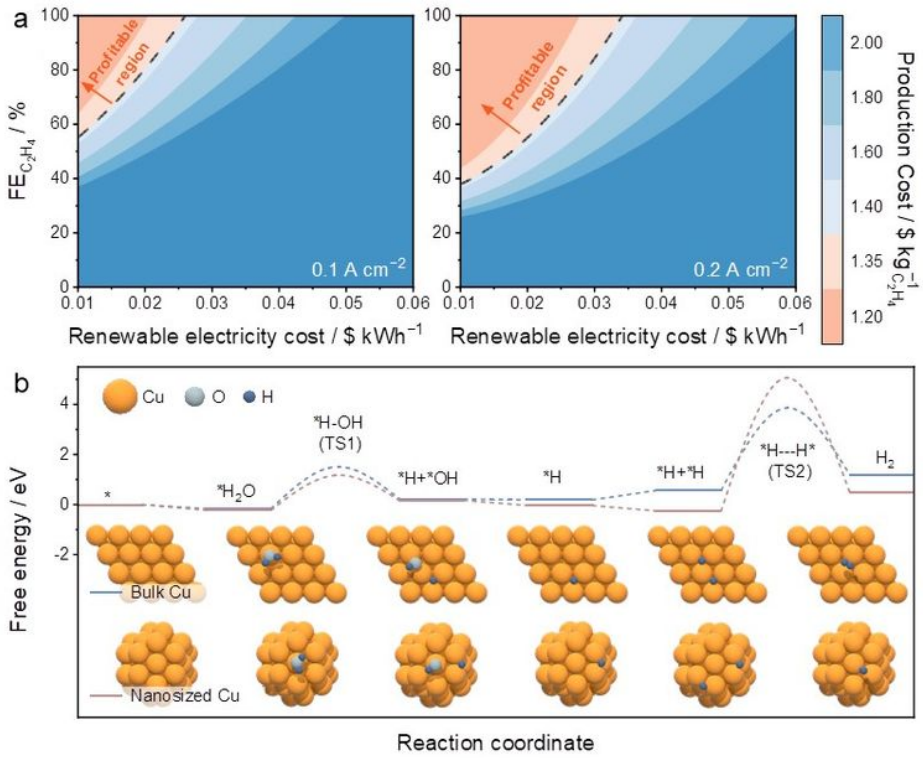

Figure 1

TEA and theoretical calculations promoting the rational design of electrodes. a TEA for C_2H_4 production of the proposed ESAE process at 0.1 and 0.2 A cm^{-2}, respectively. **b** Free-energy diagram for the water splitting process over bulk and nanosized particles.

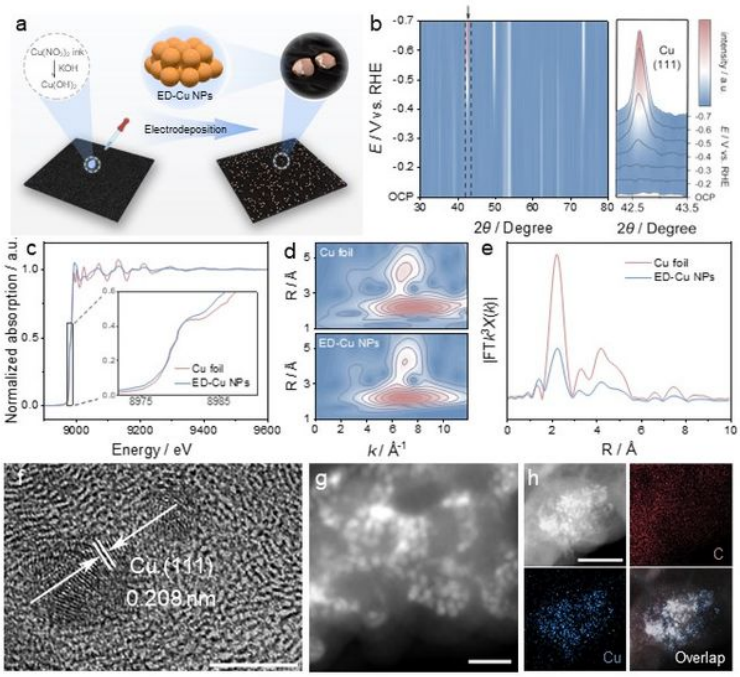

Figure 2

In situformation of ED-Cu NPs from electrodeposition of copper nitrate. a Scheme illustrating the synthesis of ED-Cu NPs via the in situ electrodeposition process of copper nitrate precursors. **b** In situ potential-dependent XRD patterns of the electrodeposition process. **c** XANES, **d** 2-D contour plots WT, and **e** EXAFS spectrum of ED-Cu NPs. The spectrum of Cu foil is also shown for comparison. **f** HRTEM, scale bars, 5 nm, **g** STEM under HAADF mode, scale bars, 20 nm, and **h** EDS element mapping images of ED-Cu NPs, scale bars, 50 nm.

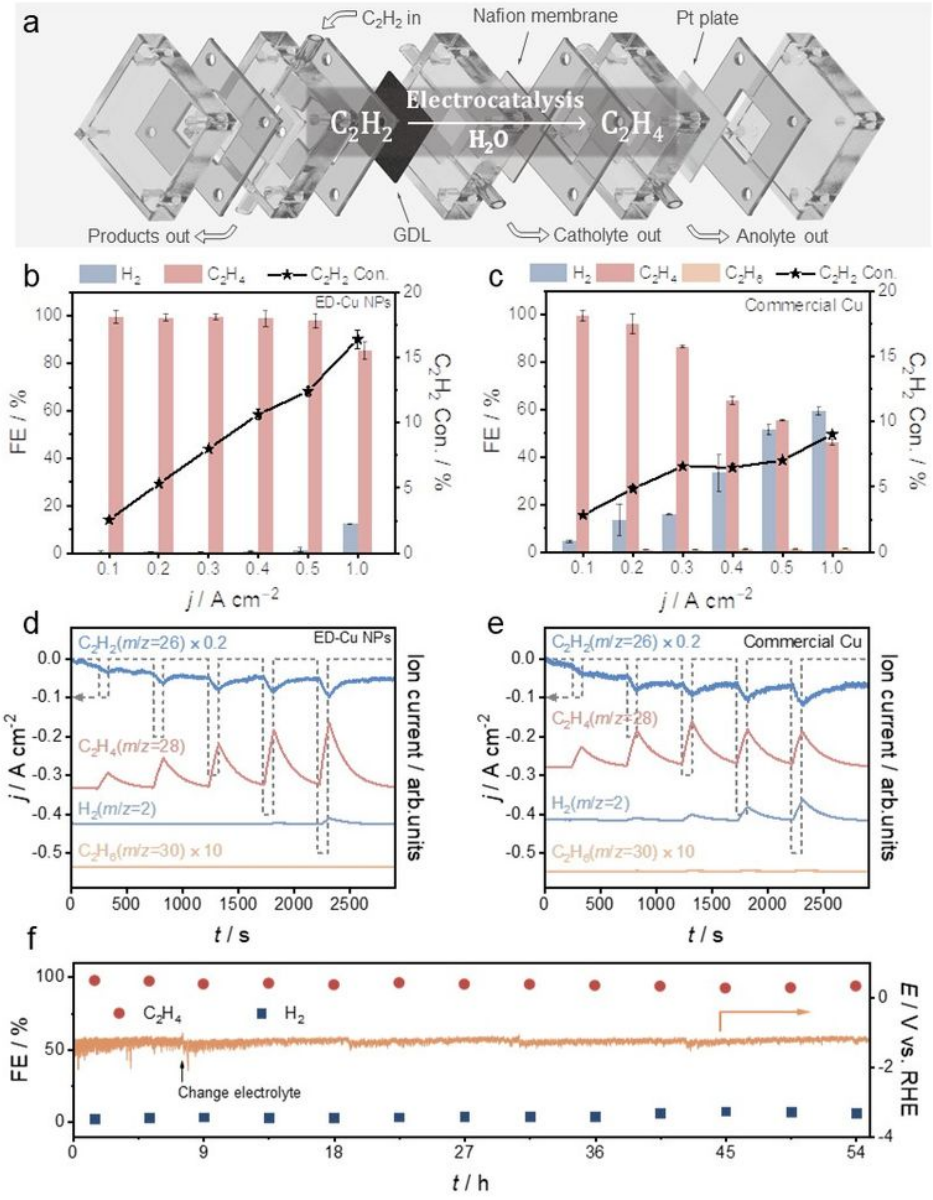

Figure 3

Performances of C_2H_4 production through the EASE process. a Schematic illustration of the flow cell applied in the performance evaluation. **b, c** Current density-dependent conversion (Con.) of C_2H_2 and FE of the obtained products over ED-Cu NPs and commercial Cu, respectively. **d, e** Operando online SFC-DEMS analysis over ED-Cu NPs and commercial Cu, respectively. **f** Continuous tests of the ED-Cu NP catalyst for the ESAE process for 54 h. Reaction conditions: 0.2 A cm^{-2}, C_2H_2 flow velocity of 30 mL min^{-1}. Error bars correspond to the standard deviation of three independent measurements, and the centre value for the error bars is the average of the three independent measurements.

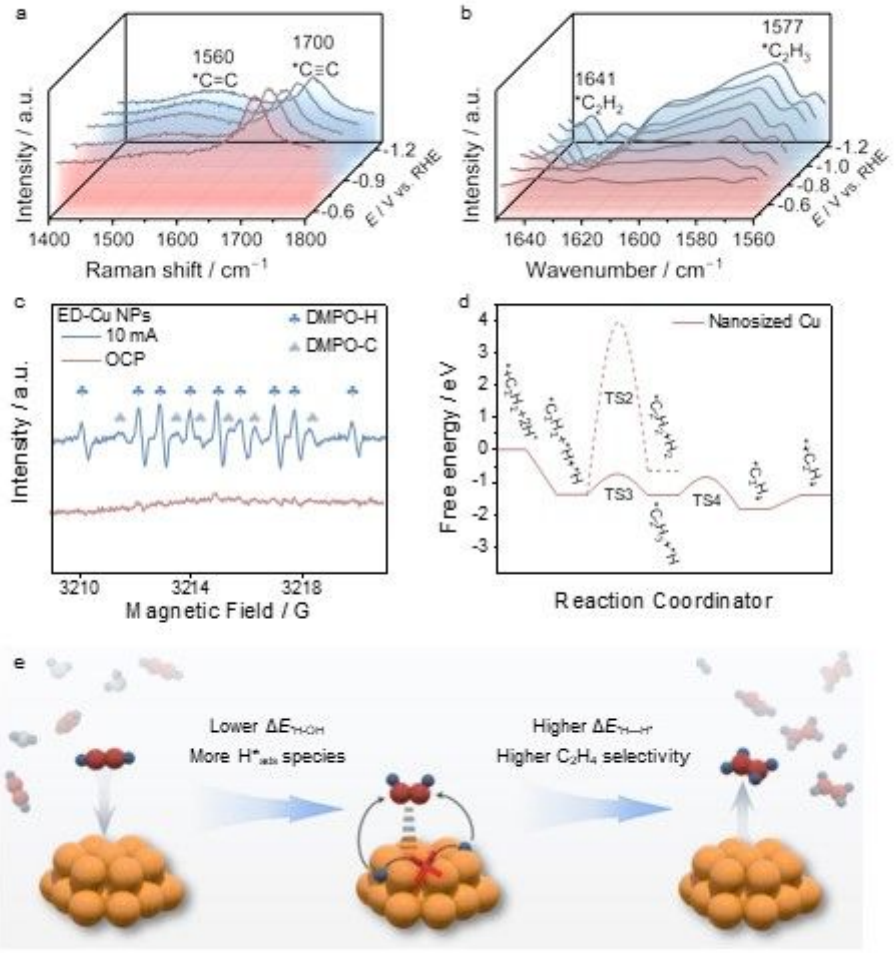

Figure 4

The hydrogenation pathway and the mechanism of enhanced C_2H_4 production. a In situ Raman spectra of ED-Cu NPs using C_2H_2 as the feeding gas. **b** In situ ATR-FTIR spectra over ED-Cu NPs in the C_2H_2-saturated electrolyte. **c** The quasi-in situ EPR trapping for hydrogen and carbon radicals over ED-Cu NPs. **d** Free-energy diagram for acetylene semihydrogenation reactions over nanosized Cu. **e** Schematic illustration of the mechanism of enhanced C_2H_4 production over ED-Cu NPs.

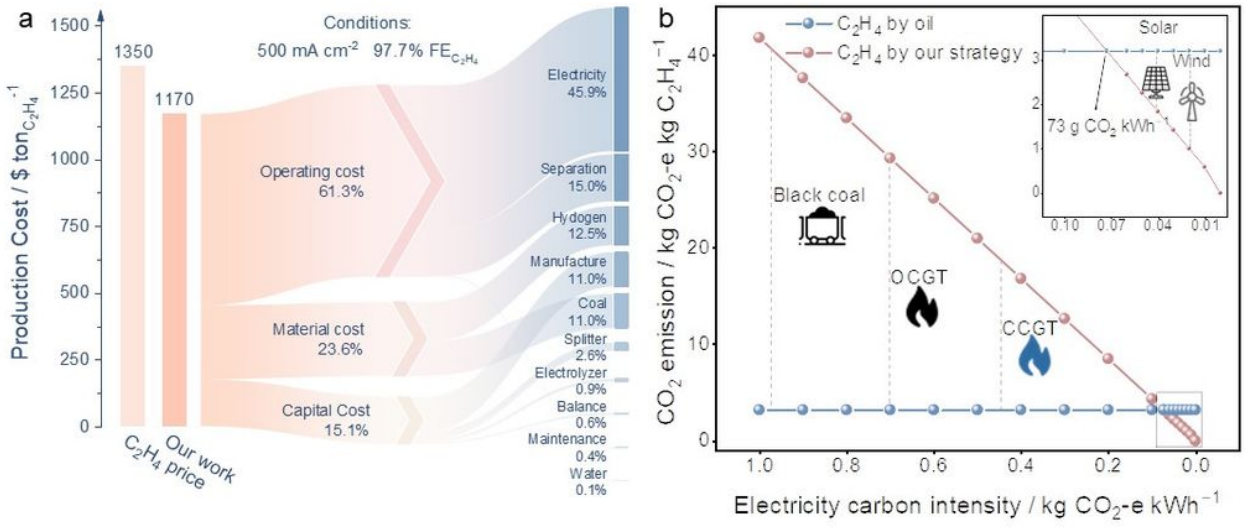

Figure 5

Sustainability evaluation of the as-proposed process. a The subdivided cost of the entire process for C_2H_4 electrosynthesis from coal-derived C_2H_2 under a current density of 0.5 A cm^{-1} at the given electricity price of 0.03 \$ kWh^{-1}. **b** The CO_2 emission of ethylene production through the EASE process of coal-derived acetylene (dark red line) with the electricity of different sources and carbon intensity and the reference CO_2 emission of ethylene production by the traditional oil route.

Supplementary Files

This is a list of supplementary files associated with this preprint. Click to download.

- SupplementaryTables.xlsx
- SupplementaryVideo1.mp4
- NatSustainSI.pdf
- SupplementaryData.xlsx
- SourcedataFig1.xlsx
- SourcedataFig2.xlsx
- SourcedataFig3.xlsx
- SourcedataFig4.xlsx

- SourcedataFig5.xlsx